CHEMISTRY
A EUROPEAN JOURNAL

DOI: 10.1002/chem.201001415

Mechanical Properties of Dense Zeolitic Imidazolate Frameworks (ZIFs): A High-Pressure X-ray Diffraction, Nanoindentation and Computational Study of the Zinc Framework $Zn(Im)_2$, and its Lithium–Boron Analogue, $LiB(Im)_4$

Thomas D. Bennett,[a] Jin-Chong Tan,[a] Stephen A. Moggach,[b] Raimondas Galvelis,[c] Caroline Mellot-Draznieks,[c] Barbara A. Reisner,[a, d] A. Thirumurugan,[a] David. R. Allan,[e] and Anthony K. Cheetham*[a]

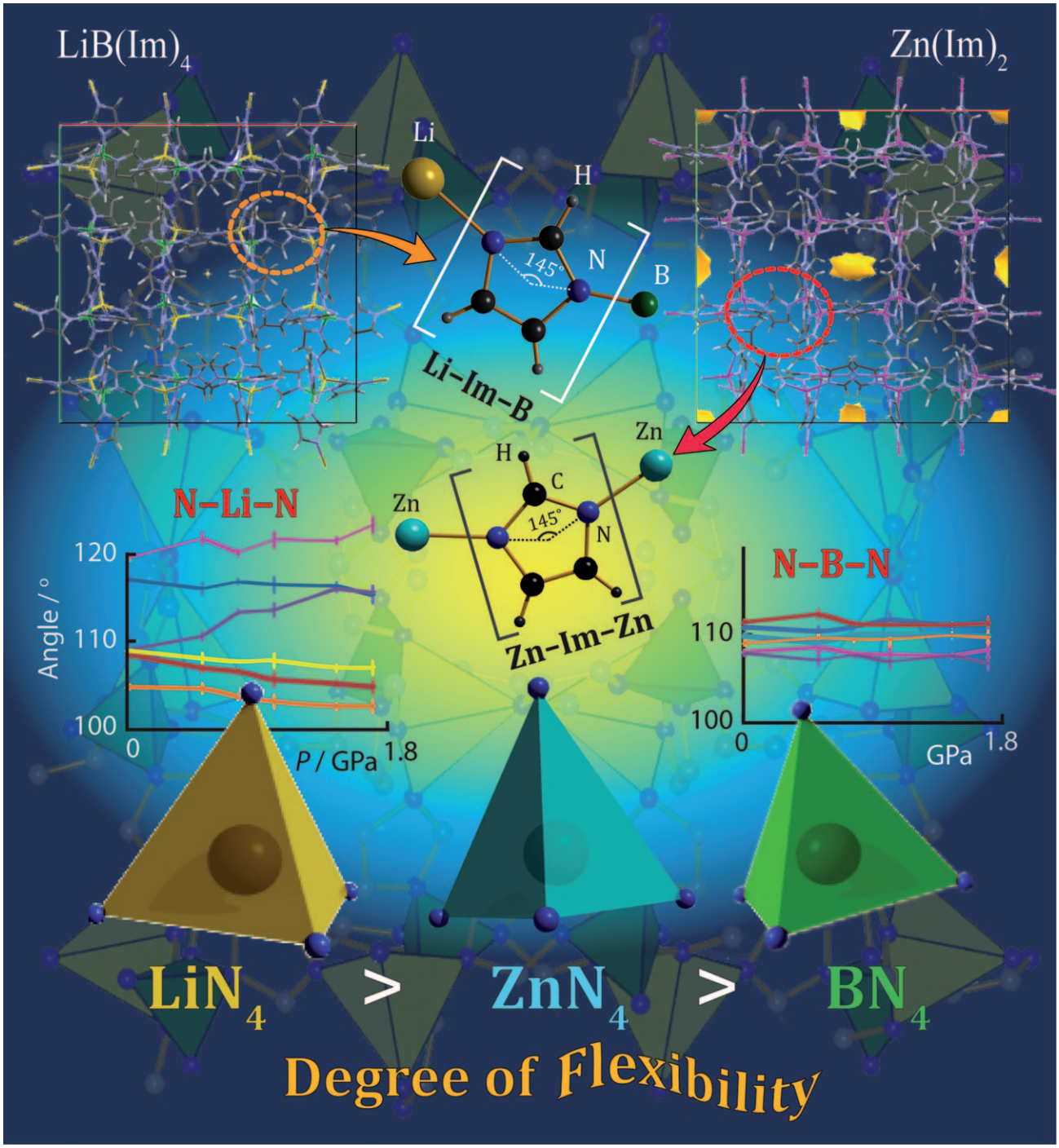

Abstract: The dense, anhydrous zeolitic imidazolate frameworks (ZIFs), $Zn(Im)_2$ (**1**) and $LiB(Im)_4$ (**2**), adopt the same zni topology and differ only in terms of the inorganic species present in their structures. Their mechanical properties (specifically the Young's and bulk moduli, along with the hardness) have been elucidated by using high pressure, synchrotron X-ray diffraction, density functional calculations and nanoindentation studies. Under hydrostatic pressure, framework **2** undergoes a phase transition at 1.69 GPa, which is somewhat higher than the transition previously reported in **1**. The Young's modulus (E) and hardness (H) of **1** ($E \approx 8.5$, $H \approx 1$ GPa) is substantially higher than that of **2** ($E \approx 3$, $H \approx 0.1$ GPa), whilst its bulk modulus is relatively lower (≈ 14 GPa cf. ≈ 16.6 GPa). The heavier, zinc-containing material was also found to be significantly harder than its light analogue. The differential behaviour of the two materials is discussed in terms of the smaller pore volume of **2** and the greater flexibility of the LiN_4 tetrahedron compared with the ZnN_4 and BN_4 units.

Keywords: mechanical properties · metal–organic frameworks · microporous materials · zeolite analogues · zeolitic imidazolate framework

Introduction

Hybrid inorganic–organic framework materials have been well documented in the literature from 1990 onwards.[1] Specifically, numerous types of metal–organic frameworks (MOFs) have been reported, including the so-called zeolitic imidazolate frameworks (ZIFs) in which tetrahedrally coordinated cations, typically zinc or cobalt, are linked by imidazolate derivatives to create topologies that are analogous to those of aluminosilicate zeolites.[2,3] The thermal stability of ZIFs is particularly striking and there is a growing literature on their potential applications in the fields of separations,[4] gas storage[5] and catalysis.[6] There is also considerable interest in dense hybrid frameworks, which have been shown to exhibit a wide range of optical, electrical and magnetic properties.[7] In the case of the ZIFs, there is a dense $Zn(Im)_2$ phase (Im = imidazolate), known by the three-letter designation zni,[8] which our density functional theory (DFT) calculations have shown to be the most stable member of the ZIF family.[9] This dense ZIF phase, which has been known for 30 years,[10] has recently been shown to undergo a pressure-induced phase transition between 0.54 and 0.85 GPa.[11] In another recent breakthrough, a family of lightweight ZIF analogues of composition $LiB(Im)_4$ has been reported.[12,13] These boron imidazolate frameworks (BIFs) are the I–III analogues of the ZIFs, with alternate Zn cations being replaced by Li and B, respectively. We have studied the mechanical properties of the Zn-containing ZIFs in considerable detail,[14] showing among other things that their Young's moduli (E) and hardnesses (H) decrease as the frameworks become more open. A thermally induced phase-transition sequence was also studied, showing that the mechanical properties of an amorphous ZIF are intermediate between those of the two bounding crystalline phases.[15] In the present work, we use a combination of high-pressure, single-crystal X-ray diffraction, nanoindentation and density functional calculations to compare the mechanical properties of the dense $Zn(Im)_2$ with its $LiB(Im)_4$ analogue.

The two topologically identical frameworks possess the same network architecture as the banalsite mineral[16] and crystallise in the tetragonal space group $I4_1cd$, with the 3D framework shown in Figure 1. We selected these structures for study because of the availability of good quality single crystals and the recent publication of the pressure-dependant behaviour of **1**.[11]

Results and Discussion

High-pressure crystallography: Studies were carried out by using a single crystal of **2** in a diamond anvil cell (DAC), surrounded by an anhydrous 2-propanol hydrostatic medium. The SQUEEZE algorithm within PLATON[17] was used to calculate the residual pore electron density after refinement, the results showing the medium to be non-invasive (see SI-1 in the Supporting Information). The evolution of the cell volume of **2** with hydrostatic pressure is shown in Figure 2a, with the discontinuity in cell volume above 1.69 GPa being indicative of a phase transition. As reported for other pressure-induced single-crystal phase transitions in

[a] T. D. Bennett, Dr. J.-C. Tan, Prof. B. A. Reisner, Dr. A. Thirumurugan, Prof. A. K. Cheetham
Department of Materials Science and Metallurgy
The University of Cambridge
Cambridge CB2 3QZ (UK)
Fax: (+44) 1223334567
E-mail: akc30@cam.ac.uk

[b] Dr. S. A. Moggach
Department of Chemistry, The University of Edinburgh
Kings Buildings, West Mains Road, Edinburgh, EH9 3JJ (UK)

[c] R. Galvelis, Dr. C. Mellot-Draznieks
Department of Chemistry, University College London
20 Gordon Street, London, WCH1 0AJ (UK)

[d] Prof. B. A. Reisner
Department of Chemistry and Biochemistry
James Madison University
Harrisonburg, VA22807 (USA)

[e] Dr. D. R. Allan
Diamond Light Source, Didcot, Oxfordshire, OX11 0DE (UK)

Supporting information for this article is available on the WWW under http://dx.doi.org/10.1002/chem.201001415.

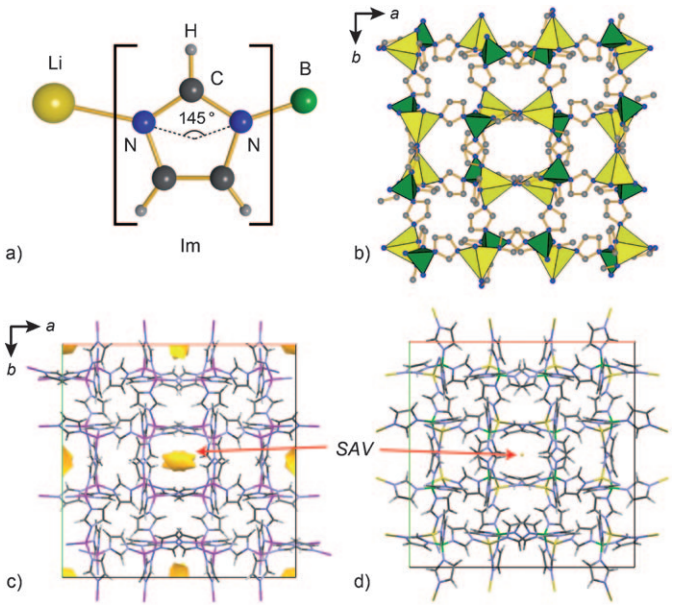

Figure 1. Structure of ZIF-zni, $Zn(Im)_2$, **1** and BIF-1-Li, $LiB(Im)_4$, **2**. a) The basic organic–inorganic connectivity of **2**. The subtended angle of 145° at the Im bridging ligand is approximately the same in each case (as in the Si-O-Si motif in zeolites), and is the reason for similar zeolitic topologies being observed in the two families. b) The unit cell of **2**, as viewed down the [001] direction. The yellow and green tetrahedra designate LiN_4 and BN_4, respectively, hydrogen atoms are omitted for clarity. c) The solvent accessible volume (SAV) of **1** viewed down the *c* axis. d) The smaller SAV detected in **2** along the same orientation. Pink: zinc, grey: carbon, blue: nitrogen, green: boron, yellow: lithium.

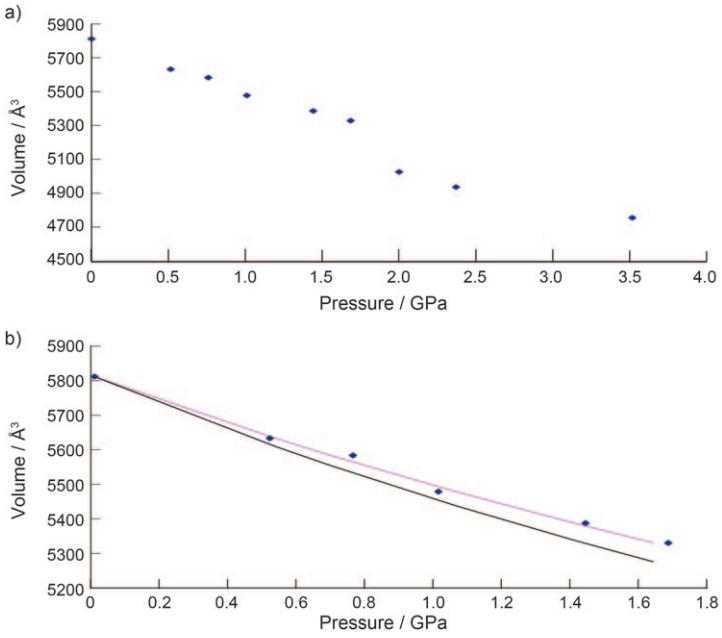

Figure 2. a) The evolution of the unit cell volume of **2** as a function of hydrostatic pressure. b) The data for the lower pressure phase, complete with the equation of state curves with bulk moduli $K_0 = 16$ GPa (pink) and $K_0 = 14$ GPa (black). $K' = 4$ in both cases.

ZIFs,[18] the transition was accompanied by extensive fracturing of the crystal (Figure 3). The decrease in data quality after 1.69 GPa rendered a full structural refinement of the irrecoverable high pressure phase impossible, though lattice parameters were obtained; the unit cell volume was found to decrease by 5.84% at the transition. The discontinuity was observed at a pressure twice that at which **1** underwent a phase transition, suggesting a qualitative increased resistance of **2** to uniform hydrostatic stress. Full details of the crystal-structure refinements up to 1.69 GPa can be found in Table 1, in which two different light sources have been used.

Table 1. Crystallographic data collection and refinement details.[a]

	Pre DAC[b]	P0[b]	P1[c]	P2[b]	P3[c]	P4[b]
P [GPa]	ambient	0.515	0.76	1.01	1.44	1.69
a [Å]	22.472	22.210	22.125	21.974	21.823	21.745
c [Å]	11.507	11.419	11406	11.346	11.3122	11.273
V [Å^3]	5811	5633	5583	5479	5388	5330
$\rho_{experimental}$ [g cm^{-3}]	1.308	1.349	1.361	1.387	1.410	1.426
collected reflns	31340	9543	26176	9153	24806	9103
unique reflns	1582	1002	1415	962	1361	930
R_{int}	0.0479	0.0975	0.0762	0.0855	0.0960	0.1045
GOF	0.9818	1.0138	0.9471	1.1406	0.9612	0.9383
R^1 [$I > 2\sigma(I)$]	0.0425	0.0588	0.0432	0.0609	0.0450	0.0593
R^2 [$I > 2\sigma(I)$]	0.0795	0.0845	0.0833	0.1257	0.0873	0.0925

[a] Crystal size $0.2 \times 0.2 \times 0.1$ mm, formula $LiBC_{12}H_{12}N_8$. Space group $I4_1cd$. All measurements at 293 K. [b] The data were collected on a laboratory X-ray source. [c] The refinement was conducted by using data collected at the DIAMOND light source.

To enable an exact comparison with the zinc analogue, an approximate determination of the bulk modulus of **2** was made by using a second-order Birch-Murnagan equation of state (Figure 2b). It was found that the data is consistent with a room-temperature K_0 value of 16.6 GPa, indicating that the framework is less compressible than **1** ($K_0 =$ 14 GPa).[11] The fit to the data by using the latter value is shown for completeness. We note that this value lies in the range expected for such dense hybrid materials, whilst lying above those found for more porous zeolitic imidazolate frameworks (e.g., ZIF-8, $K_0 \approx 6.5$ GPa).[19]

The greater resistance to uniform compression of **2** may be rationalised by the lighter framework having a lower porous volume, thereby rendering it less able to accommodate volumetric strains induced by the hydrostatic stress field. Although it is isostructural, the cell volume of **1** is around 23% larger than that of **2** (6883.1 Å^3 cf. 5583.3 Å^3), with the solvent accessible volume (SAV) within each framework being 12.2 and 5.3%, respectively, see Figure 1c and d (as calculated by using PLATON).[17]

As in the study of **1**, it can be demonstrated that there is no significant change in either Li–N or B–N bond lengths upon increasing the hydrostatic pressure (see SI-2 in the Supporting Information). A consideration of N-B-N angular distortions yields a similarly rigid picture, but the LiN_4 tetrahedra show a markedly greater deformation (Figure 4), even

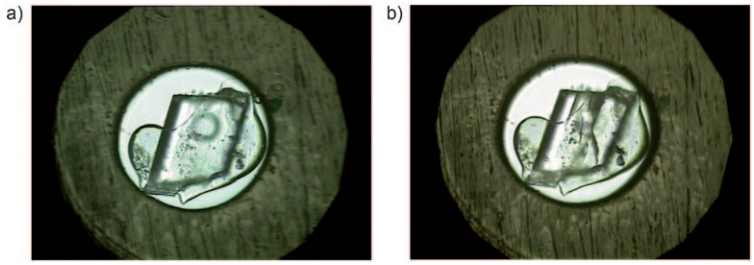

Figure 3. $LiB(Im)_4$ single crystal in the DAC before (a) and after (b) the phase transition. The fracturing caused by the transition is evident. Gasket size 300 μm.

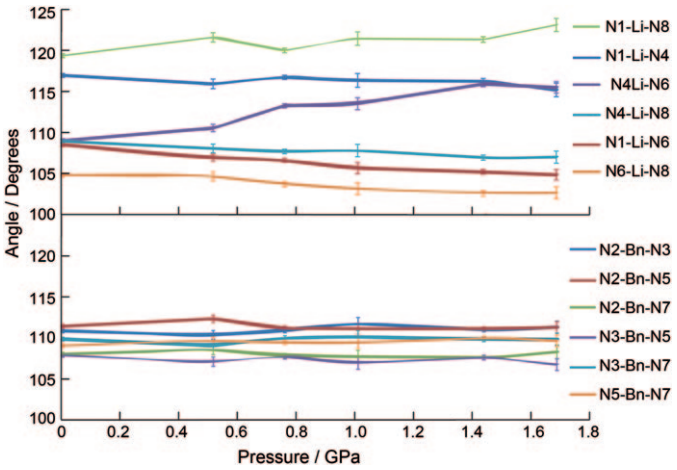

Figure 4. The evolution of bond angles around the central metal atom with increasing pressure. The LiN_4 tetrahedra can be clearly seen to be more deformable than the BN_4 tetrahedra. The numerals 1 to 8 denote the crystallographically independent imidazolate nitrogen atoms present in the framework.

when compared to changes in the N-Zn-N bond angles reported previously for **1**. Indeed, a direct comparison of the spread of N-M-N angles (M = metal) at each pressure indicates that the ZnN_4 tetrahedra lie between the lithium and boron equivalents in terms of flexibility (see SI-3 in the Supporting Information). These results demonstrate the softer, more deformable nature of the lithium coordination environment, and are intuitive, in view of both the metal–nitrogen bond length and the lower valence of the metal ion.

Computational studies: DFT calculations were performed to optimise the two structures at pressures of 0 and 0.5 GPa to enable comparison with the experimental results. Note that these are the only two pressures at which data is available for both **1** and **2**. Generalised gradient approximation (GGA) based the Perdew-Burke-Ernzerhof (PBE)[20] exchange–correlation functional with a semi-empirical long-range dispersive-force correction (the so-called PBE-D)[21] was used to relax atomic positions and unit cell parameters without any symmetry constraints (*P*1 symmetry). A comparison of simulated and experimental lattice parameters, along with fractional atomic coordinates, are given in SI-4 and SI-5 in the Supporting Information. The simulated values show excellent agreement with the experimentally derived data. The agreement is all the more impressive, bearing in mind the structural complexity of the materials studied (> 500 atoms in the unit cell), and that the simulations were performed at 0 K.

Subsequent statistical analysis of the M–N bond lengths present in the optimised structures show little significant change upon pressurisation, though the intermediate flexibility of the zinc environment does present itself here, and the lengths decrease at a rate between that of the Li–N and B–N bonds (see SI-6 in the Supporting Information). The distribution of N-M-N bond angles provides a far more significant insight into the differential behaviour of the framework materials, in an almost identical fashion to the results drawn from the experimental study. Mean N-M-N bond angles and their corresponding spreads are presented in Table 2, alongside the experimentally determined values, and it is again clear that the sequence of flexibility has been established as $LiN_4 > ZnN_4 > BN_4$.

Table 2. Summary of the mean and distribution of the N-M-N bond angles with increasing pressure, calculated by DFT whereby the standard deviations were derived from the entire population used in the computation (see SI-7 in the Supporting Information). Experimental values are in italics and agree well with the computational results.

Pressure [GPa]	Bond angles [°]		
	N-Zn-N	N-Li-N	N-B-N
0	109.23 ± 3.99	110.40 ± 6.07	109.47 ± 1.20
0.5	109.18 ± 4.85	110.35 ± 6.58	109.47 ± 1.15
0	*109.35 ± 6.0*	*109.29 ± 7.27*	*109.47 ± 1.69*
0.515	–	*109.31 ± 8.47*	*109.47 ± 2.60*
0.54	*109.33 ± 7.7*	–	–

The bulk moduli (K) approximated from the theoretical calculations also agree very well with the experiments, yielding 13.25 and 16.54 GPa for **1** and **2**, respectively,[22] compared with experimental values of ≈14[11] and ≈16.6 GPa, respectively.[23] The lighter framework of **2** has again been shown to be less compressible, despite evidence to the contrary in the flexibility of the LiN_4 tetrahedra.

Nanoindentation studies: The E and H properties of single crystals of **1** and **2** were determined by means of nanoindentation experiments performed at ambient conditions. Importantly, we note that unlike hydrostatic compression, the crystal surfaces are not fully constrained and hence the indentation stress field generated is not purely hydrostatic.[24] It has been recently established that such an indentation stress state can be used to probe the anisotropic mechanical prop-

erties of hybrid crystals[25,26] because the measured modulus is strongly dependent upon the elastic response along the indenter axis and is only weakly affected by the transverse directions.

Figure 5a shows the representative indentation curves obtained by probing the {100}- and {001}-oriented facets (see the inset of Figure 5a). They are generated by directional

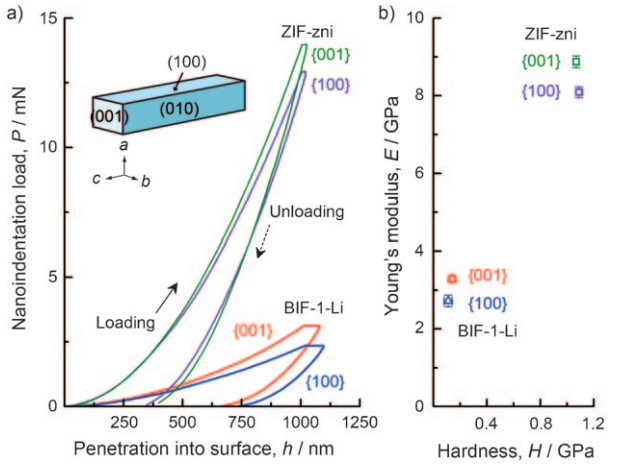

Figure 5. Nanoindentation results of ZIF-zni **1** and BIF-1-Li **2**. a) Representative nanoindentation load versus displacement curves measured along the {100}- and {001}-oriented crystal facets for a maximum indentation depth of 1000 nm. The inset illustrates the typical habit of the single crystals. b) The average values of Young's moduli and hardness properties, whereby the error bars denote the standard deviations determined from 15 indentation experiments.

compressive strains transmitted from the sharp-tipped indenter oriented along the *a* and *c* axes, respectively. The gradient of the initial unloading segment signifies the Young's modulus of the material, which is a measure of the intrinsic stiffness of the underlying framework along a chosen direction. In Figure 5b, we show that the Young's moduli of **1** ($E \approx 8$ to 9 GPa) are in fact three times greater than those of the lightweight counterpart **2** (2.7 to 3.3 GPa). Because both frameworks have the same topology, the large difference in terms of their moduli indicates that the Zn–Im–Zn bonds of **1** are considerably stiffer than the predominantly ionic bonds associated with the Li–Im–B linkages of **2**. In addition, we note that their tetragonal symmetry also gives rise to elastic anisotropy, whereby the ratios of $E_{\{001\}}$:$E_{\{100\}}$ were found to lie in the range of 1.1 to 1.2. It can be seen that the *c* axis is relatively more stiff for both frameworks, and this corresponds to the orientation down the "channels" depicted in Figure 1c and d.

Under the indentation stress field, we note that the maximum load and hence the hardness property measured by the nanoindenter vary greatly between the two isostructural frameworks. As depicted in Figure 5a, it can be seen that **1** can develop substantially higher loads at the maximum indentation depth, of up to five times larger than its lightweight analogue. The hardness of **2** was found to be at $\approx$150 MPa (Figure 5b), almost an order of magnitude lower than that found in the denser **1** ($H \approx 1.1$ GPa). Our results indicate that the lighter framework exhibits a significantly lower resistance towards permanent plastic deformation (attributed to shear stresses generated by the nanoindenter tip),[26] a striking result when compared with the earlier finding that **2** has a higher bulk modulus.

We have previously illustrated the relative deformation of each metal polyhedra (see Figure 4 and Table 2), concluding that LiN_4 is indeed the more flexible and compliant motif. Although the stress field conditions in the probing of the Young's modulus are different (strongly directional and somewhat more uniaxial compared with purely uniform hydrostatic), we suggest that it is the relative ease with which the LiN_4 tetrahedra can flex that dominates the Li–Im–B linkage response under an indentation stress field, giving rise to the strikingly lower *E* and *H* values for framework **2**. In contrast, the zinc coordination environment found at both ends of the Zn–Im–Zn linkages has been shown to be more robust to externally applied stresses and strains.

Conclusion

We report a surprising result in the mechanical properties of two isostructural dense hybrid frameworks. We conclude that even though $LiB(Im)_4$ is less compressible than $Zn(Im)_2$, it has a substantially lower Young's modulus. It is apparent from both experimental and simulated structures in **2** that the BN_4 tetrahedra are intrinsically more constrained than the LiN_4 tetrahedra, and thus the flexibility and deformations in **2** are born by the LiN_4 tetrahedra exclusively. Such features are clearly not present in the uni-nodal crystal structure of **1**.

Interesting comparisons can be drawn between the scenario outlined here and that of α-quartz (SiO_2) and berlinite ($AlPO_4$). In the latter case, experimental bulk moduli are again comparable at around 37 GPa,[27–29] whereas the Young's moduli of the mixed metal framework are approximately 20% lower.[30] In the same way as the highly flexible LiN_4 species lowered the elastic modulus of **2**, it appears here that the reason for the lower elastic modulus of berlinite is down to the presence of the more flexible AlO_4 tetrahedron ($AlO_4 > SiO_4 > PO_4$). Hence, we conclude that the rationale observed and explained here is likely to be a general one, thus giving us a useful rule-of-thumb for predicting the mechanical properties of the myriad of MOF materials.

We could also draw another very important conclusion from our work, on the basis of the mechanical hardness results. As shown in Figure 5, the hardness of **2** is an order of magnitude lower than that of **1**, a result that we again attribute to the lower bond energies associated with the LiN_4 tetrahedra. Although BN_4 tetrahedra are associated with higher bond energies, it is the weaker lithium coordination environment that allows the framework to deform with applied load, therefore contributing most to the hardness. In light of this, we hypothesise that the same should be true of

other lightweight BIF frameworks that incorporate flexible linkages. Notably, low hardness properties can give rise to substantial and irreversible plastic deformation when subjected to external stresses beyond the elastic strains. It follows that BIF-type materials may not be as good as their zinc analogues for applications that push the materials beyond their elastic limits.

Experimental Section

Synthesis

$LiB(Im)_4$ (BIF-1-Li): $Li(OH)\cdot H_2O$ (0.004 g, 1×10^{-4} mol) and $NaB(Im)_4$ (0.03 g, 1×10^{-4} mol) were added to butan-1-ol (6 mL). The resultant solution was placed in a 23 mL Teflon-lined autoclave and heated to 100 °C for 7 days in a programmable oven, before cooling to room temperature at a rate of 5 °C h^{-1}. Rod-shaped single crystals were isolated from the mother liquor by filtration, washed with dichloromethane (5 mL × 2) and air-dried.

$Zn(Im)_2$ (ZIF-zni): A solution of zinc nitrate hexahydrate $Zn(NO_3)_2\cdot 6H_2O$ in DMF (2 mL, 4×10^{-3} mol) was combined with sodium boron imidazolate $NaB(Im)_4$ (0.12 g, 4×10^{-3} mol) and DMF (5 mL). The resultant solution was placed in a 23 mL Teflon-lined autoclave and heated to 180 °C for 72 h in a programmable oven, before cooling to room temperature at a rate of 5 °C h^{-1}. Rod-shaped single crystals were isolated from the mother liquor by filtration, washed with dichloromethane (5 mL × 2) and air-dried.

High-pressure crystallography: A sphere of data was collected on a crystal of $LiB(Im)_4$ at ambient temperature and pressure to provide data for comparison with the high-pressure studies, which were also performed at ambient temperature (see below). Diffraction data were collected on a Bruker SMART APEX diffractometer with graphite-monochromated $Mo_{K\alpha}$ radiation ($\lambda = 0.71073$ Å). These data were integrated by using the program SAINT,[31] whereas the absorption correction was carried out by using the program SADABS.[32] Refinement was carried out against $|F|^2$ by using all data[33] starting from the ambient-temperature coordinates of Zhang et al.[12] The final conventional R factor was 0.0425 for 1444 reflections. High-pressure diffraction data was then collected on the same crystal, again on a Bruker SMART APEX diffractometer ($\lambda = 0.71073$ Å). Data were collected in ω scans in eight settings of 2θ and ϕ with a frame time and step size of sixty seconds and 0.3°, respectively. This data collection strategy was based on that described by Dawson et al.[34] High-pressure data were also collected on a different crystal of $LiB(Im)_4$ at the DIAMOND light source on station I19 on a Crystal Logic four-circle goniometer equipped with a Rigaku Saturn 724 CCD detector ($\lambda = 0.5159$ Å). Data were collected in ω and ϕ scans in twelve settings of 2θ and ϕ with a frame time and step size of one second and 0.5°, respectively. All high-pressure data were integrated by using the program SAINT that used "dynamic masks" to avoid integration of regions of the detector that were shaded by the body of the pressure cell. Absorption corrections for the DAC and sample were carried out with the programs SHADE and SADABS, respectively. Data were collected from 0.52 GPa up to a final pressure of 3.5 GPa.

Refinements of $LiB(Im)_4$ were carried out against $|F|^2$ by using all data. For high-pressure data collected on the Bruker SMART APEX diffractometer, all 1,2 and 1,3 distances on the imidazolate ions were restrained to the values observed from our ambient-pressure structure. Similarity restraints were applied to Li–N and B–N distances, whereas all torsion angles were refined freely. Hydrogen atoms attached to carbon were placed geometrically and not refined. Thermal similarity restraints were applied to all non-hydrogen atoms. For the synchrotron data sets, no restraints were applied. This parameterisation strategy was utilised owing to the reduced completeness of high-pressure data that was collected by using longer wavelength X-rays, caused by shading from the pressure cell. On increasing pressure to 1.67 GPa, all Li, B, C and N atoms were refined with anisotropic thermal parameters. Above 1.67 GPa, the crystal underwent a phase transition, which resulted in the crystal breaking apart and becoming polycrystalline.

DFT calculations: The computational study was performed with CP2 K[35] code using the linear scaling DFT module Quickstep.[36] A restricted Kohn–Sham (KHS) formalism and GGA-based PBE[20] exchange-correlation functional with a semi-empirical long-range dispersive force correction[21] were used. Electronic energy was minimised with orbital transformation with a direct inversion in the iterative subspace (OT/DIIS)[37] method. The convergence criteria for self-consistent field (SCF) procedure was set to 1.0×10^{-7} a.u.

The nuclear and core electronic density were modelled with Goedecker-Teter-Hutter (GTH)[38,39] pseudo-potentials and valence electronic density represented by a dual Gaussian basis sets and plane wave (GPW) scheme.[40] All atoms had molecular optimised DZVP basis sets[41] and the plane wave cut off was 400 Ry. Crystallographic unit cells with periodic boundary conditions (PBC) and Γ-point sampling were used.

Optimisations were started from experimental structures at 0 GPa pressure in $P1$ symmetry and were carried out until convergence criteria (atomic positions: maximum displacement 3.0×10^{-4} a.u., RMS (root-mean-square) displacement 1.5×10^{-4} a.u., maximum force 4.5×10^{-4} a.u. and RMS force 3.0×10^{-5} a.u.; cell parameters: maximum displacement 3.0×10^{-3} a.u., RMS displacement 1.5×10^{-3} a.u., maximum force 4.5×10^{-4} a.u., RMS force 3.0×10^{-4} a.u. and pressure deviation 0.01 GPa) were met.

Single-crystal nanoindentation: E and H mechanical properties were measured by using an MTS Nanoindenter XP at ambient conditions. The Miller indices of the tetragonal crystals (Figure 5, inset) were first identified by using single-crystal X-ray diffraction, prior to mounting in an epoxy resin and followed by diamond polishing to attain an RMS surface roughness of <10 nm (confirmed by atomic force microscopy). Indentation experiments were performed under the dynamic displacement controlled mode, at a constant strain rate of 0.05 s^{-1}. All tests were conducted by using a three-sided pyramidal (Berkovich) diamond indenter tip to a maximum surface penetration depth of 1000 nm. The indenter axis was oriented normal to the crystal facets, that is, along the a, b and c axes, to determine the extent of mechanical anisotropy. The load–displacement data collected were analysed by using the Oliver and Pharr method, described in reference [42].

Acknowledgements

We thank the Royal Society of Edinburgh and the Scottish government for a Personal Research Fellowship (to S.A.M.), along with the James Madison University Program of Grants for Faculty Assistance (to B.A.R.) We also thank the E.P.S.R.C., UK for funding (T.D.B., C.M.-D. and R.G.) and the European Research Council (J.C.T., A.T. and A.K.C.). The authors acknowledge the use of the UCL Legion High Performance Computing Facility and associated support services in completion of this work, and also DIAMOND for provision of synchrotron time.

[1] B. F. Hoskins, R. Robson, *J. Am. Chem. Soc.* **1990**, *112*, 1546–1554.
[2] Y. Q. Tian, C. X. Cai, X. M. Ren, C. Y. Duan, Y. Xu, S. Gao, X. Z. You, *Chem. Eur. J.* **2003**, *9*, 5673–5685.
[3] K. S. Park, Z. Ni, A. P. Cote, J. Y. Choi, R. D. Huang, F. J. Uribe-Romo, H. K. Chae, M. O'Keeffe, O. M. Yaghi, *Proc. Natl. Acad. Sci. USA* **2006**, *103*, 10186–10191.
[4] K. Li, D. H. Olson, J. Seidel, T. J. Emge, H. Gong, H. Zeng, J. Li, *J. Am. Chem. Soc.* **2009**, *131*, 10368–10369.
[5] R. E. Morris, P. S. Wheatley, *Angew. Chem.* **2008**, *120*, 5044–5059; *Angew. Chem. Int. Ed.* **2008**, *47*, 4966–4981.
[6] H.-L. Jiang, B. Liu, T. Akita, M. Haruta, H. Sakurai, Q. Xu, *J. Am. Chem. Soc.* **2009**, *131*, 11302–11303.
[7] C. N. R. Rao, A. K. Cheetham, A. Thirumurugan, *J. Phys. Condens. Matter* **2008**, *20*, 159801.

[8] M. O'Keeffe, M. A. Peskov, S. J. Ramsden, O. M. Yaghi, *Acc. Chem. Res.* **2008**, *41*, 1782–1789.
[9] D. W. Lewis, A. R. Ruiz-Salvador, A. Gomez, L. M. Rodriguez-Albelo, F. X. Coudert, B. Slater, A. K. Cheetham, C. Mellot-Draznieks, *CrystEngComm* **2009**, *11*, 2272–2276.
[10] F. Seel, R. Lehnert, E. Bill, A. Trautwein, *Z. Naturforsch. B* **1980**, *35*, 631–638.
[11] E. C. Spencer, R. J. Angel, N. L. Ross, B. E. Hanson, J. A. K. Howard, *J. Am. Chem. Soc.* **2009**, *131*, 4022–4026.
[12] H. Zhang, T. Wu, C. Zhou, S. M. Chen, P. Y. Feng, X. H. Bu, *Angew. Chem.* **2009**, *121*, 2580–2583; *Angew. Chem. Int. Ed.* **2009**, *48*, 2542–2545.
[13] T. Wu, J. Zhang, C. Zhou, L. Wang, X. H. Bu, P. Y. Feng, *J. Am. Chem. Soc.* **2009**, *131*, 6111–6113.
[14] J. C. Tan, T. D. Bennett, A. K. Cheetham, *Proc. Natl. Acad. Sci. USA* **2010**, *107*, 9938–9943.
[15] T. D. Bennett, A. L. Goodwin, M. T. Dove, D. A. Keen, M. G. Tucker, E. R. Barney, A. K. Soper, E. G. Bithell, J. C. Tan, A. K. Cheetham, *Phys. Rev. Lett.* **2010**, *104*, 115503.
[16] R. P. Liferovich, A. J. Locock, R. H. Mitchell, A. K. Shpachenko, *Can. Mineral.* **2006**, *44*, 533–546.
[17] A. L. Spek, *PLATON: A Multipurpose Crystallographic Tool*; Utrecht University, Utrecht (The Netherlands), **2004**.
[18] S. A. Moggach, T. D. Bennett, A. K. Cheetham, *Angew. Chem.* **2009**, *121*, 7221–7223; *Angew. Chem. Int. Ed.* **2009**, *48*, 7087–7089.
[19] K. W. Chapman, G. J. Halder, P. J. Chupas, *J. Am. Chem. Soc.* **2009**, *131*, 17546–17547.
[20] J. P. Perdew, K. Burke, M. Ernzerhof, *Phys. Rev. Lett.* **1996**, *77*, 3865–3868.
[21] S. Grimme, *J. Comput. Chem.* **2006**, *27*, 1787–1799.
[22] The bulk modulus (K) is defined by $-V(\mathrm{d}P/\mathrm{d}V)$, in which P and V are the applied pressure and cell volume, respectively. Because the DFT calculation was performed at only two pressure points (0 and 0.5 GPa), the gradient ($\mathrm{d}P/\mathrm{d}V$) is simply given by a linear relationship established over that range. Based on the cell volumes at 0 and 0.5 GPa, for **1**, we obtained the corresponding K values of 13.5 and 13.0 GPa, respectively. We reported the mean value as 13.25 GPa because the pressure range considered here is relatively small. The same applies to **2**.
[23] For direct comparison with DFT, the experimental K value of **2** was determined over a reduced pressure range, covering only two pressure points at 0 and 0.515 GPa. The modulus found is $\approx$0.6 GPa larger than that determined from the second-order Birch-Murnagan equation of state ($K_0 = 16$ GPa).
[24] A. C. Fisher-Cripps, *Nanoindentation*, Springer, New York, **2004**, pp. 39–68.
[25] J. C. Tan, J. D. Furman, A. K. Cheetham, *J. Am. Chem. Soc.* **2009**, *131*, 14252–14254.
[26] J. C. Tan, J. B. Orton, C. A. Merrill, A. K. Cheetham, *Acta Mater.* **2009**, *57*, 3481–3496.
[27] S. M. Sharma, N. Garg, S. K. Sikka, *J. Phys. Condens. Matter* **2000**, *12*, 6683–6692.
[28] D. M. Christie, J. R. Chelikowsky, *Phys. Chem. Miner.* **1998**, *25*, 222–226.
[29] E. Calderon, M. Gauthier, F. Decremps, G. Hamel, G. Syfosse, A. Polian, *J. Phys. Condens. Matter* **2007**, *19*, 436228.
[30] T. Hanada, Y. Bessyo, N. Soga, *J. Non-Cryst. Solids* **1989**, *113*, 213–220.
[31] Bruker-Nonius, Bruker-AXS, Madison, Wisconsin, **2006**.
[32] SADABS Version 2004/1, G. M. Sheldrick, Bruker-AXS, Madison, Wisconsin, **2004**.
[33] P. W. Betteridge, J. R. Carruthers, R. I. Cooper, K. Prout, D. J. Watkin, *J. Appl. Crystallogr.* **2003**, *36*, 1487.
[34] A. Dawson, D. R. Allan, S. Parsons, M. Ruf, *J. Appl. Crystallogr.* **2004**, *37*, 410–416.
[35] CP2K Developers Page: http://cp2k.berlios.de.
[36] J. VandeVondele, M. Krack, F. Mohamed, M. Parrinello, T. Chassaing, J. Hutter, *Comput. Phys. Commun.* **2005**, *167*, 103–128.
[37] J. VandeVondele, J. Hutter, *J. Chem. Phys.* **2003**, *118*, 4365–4369.
[38] S. Goedecker, M. Teter, J. Hutter, *Phys. Rev. B* **1996**, *54*, 1703–1710.
[39] M. Krack, *Theor. Chem. Acc.* **2005**, *114*, 145–152.
[40] G. Lippert, J. Hutter, M. Parrinello, *Mol. Phys.* **1997**, *92*, 477–487.
[41] J. VandeVondele, J. Hutter, *J. Chem. Phys.* **2007**, *127*, 114105.
[42] W. C. Oliver, G. M. Pharr, *J. Mater. Res.* **2004**, *19*, 3–20.

Received: May 21, 2010
Published online: August 30, 2010

